Multiscale clustering of heavy and light small particles in turbulent channel flow at high Reynolds numbers

Yutaro Motoori, Susumu Goto

Graduate School of Engineering Science, Osaka University, 1-3 Machikaneyama, Toyonaka, Osaka, 560-8531, Japan

ARTICLE INFO

Keywords:
Particle clustering
Turbulent channel flow
Hierarchy of vortices

ABSTRACT

To understand the fundamental mechanism of the clustering of heavy and light small particles in high-Reynolds-number wall turbulence, we conduct direct numerical simulations of particle dispersions in turbulent channel flow at the friction Reynolds number $Re_\tau = 2000$. Heavy and light particles form clusters with different shapes, and the cluster size is larger for particles with longer relaxation time. To reveal the origin of these multiscale clusters of particles, we investigate particle distributions around multiscale vortices. Vortices tend to sweep out heavy particles and tend to attract light ones with a relaxation time comparable with their turnover time. These clustering phenomena due to coherent vortices can occur irrespective of their size, existing height and the friction Reynolds number. We can therefore explain the multiscale nature of particle clustering in terms of the time scale matching between particles and vortices.

1. Introduction

We investigate the behaviour of heavy and light small particles in wall turbulence at high Reynolds numbers. Since the transport of heavy small particles is related to various natural and engineering systems such as the formation of rain droplets (Vaillancourt and Yau, 2000; Shaw, 2003; Saito and Gotoh, 2018; Matsuda, Schneider and Yoshimatsu, 2021), sediments at the bottom of rivers (Seminara, 2010; Scherer, Uhlmann, Kidanemariam and Krayer, 2022) and aggregation of particles in combustion engines (Guzzella and Onder, 2009), there are a substantial number of fundamental studies on the turbulent transport of heavy particles in homogeneous isotropic turbulence (Riley and Patterson, 1974; Squires and Eaton, 1990, 1991; Yeung, 2002; Yoshimoto and Goto, 2007; Toschi and Bodenschatz, 2009; Balachandar and Eaton, 2010; Monchaux, Bourgoin and Cartellier, 2012; Gustavsson and Mehlig, 2016; Oka and Goto, 2021), which is a model of turbulence away from the wall, and in near-wall turbulence (Caporaloni, Tampieri, Trombetti and Vittori, O., 1975; Reeks, 1983; Marchioli and Soldati, 2002; Marchioli, Giusti, Salvetti and Soldati, 2003; Narayanan, Lakehal, Botto and Soldati, 2003; Picciotto, Marchioli and Soldati, 2005; Picano, Sardina and Casciola, 2009; Soldati and Marchioli, 2009; Sardina, Schlatter, Brandt, Picano and Casciola, 2012; Bernardini, 2014; Johnson, Bassenne and Moin, 2020; Brandt and Coletti, 2022).

In the near-wall region, the turbulent transport of heavy particles is well described in terms of coherent flow structures (Soldati and Marchioli, 2009); when the relaxation time of the particles is comparable with the turnover time of streamwise vortices in the buffer layer, the particles tend to be swept out from the vortex core. Then, these particles are accumulated in low-speed streaks accompanied by the streamwise vortices. In other words, since there is no scale separation in turbulence at low Reynolds numbers, particles whose relaxation time is a few dozen wall-unit time-scales (i.e. eddy turnover time of streamwise vortices) form clusters.

As the Reynolds number increases, in addition to the buffer-layer coherent structures, multiscale flow structures can contribute to transporting particles. Our previous study (Motoori, Wong and Goto, 2022) showed that, by conducting direct numerical simulations (DNS) of heavy small particles in turbulent channel flow at the friction Reynolds number $Re_\tau = 1000$, particles with different relaxation times form clusters with different sizes. The clusters are formed around vortices whose turnover time is comparable with the relaxation time of particles. In particular, while wall-detached vortices sweep out the particles isotropically, wall-attached streamwise vortices tend to sweep out particles toward nearby low-speed streaks with the same size as the vortices. As a result, near the wall, we observe multiscale streamwise-elongated particle concentrations. Similar multiscale clusters in multiscale streaks were also numerically observed by Jie, Cui, Xu and Zhao (2022). Recent experiments (Berk and Coletti, 2020) on heavy small particles in turbulent boundary layers also showed that particles preferentially concentrate in ejection events for a wide range of the particle relaxation time. Incidentally, the multiscale clusterings due to wall-detached vortices are similar to those observed in turbulence in a periodic cube (Oka and Goto, 2021).

On the other hand, many laboratory experiments demonstrated that light particles, such as air bubbles in water, tend to be accumulated in the core of vortices (Douady, Couder and Brachet, 1991; Park, Saito, Tasaka and Murai, 2019). Numerical studies also showed the clustering phenomena such as in homogeneous isotropic turbulence (Calzavarini, Kerscher, Lohse and Toschi, 2008; Tagawa, Mercado, Prakash, Calzavarini, Sun and Lohse, 2012) and in turbulent channel flow (Lakehal, Métrailler and Reboux, 2017; Zhai, Fairweather and Colombo, 2020). Recently, we (Oka, Watanabe and Goto, 2021) also conducted DNS of

y.motoori.es@osaka-u.ac.jp (Y. Motoori);
s.goto.es@osaka-u.ac.jp (S. Goto)

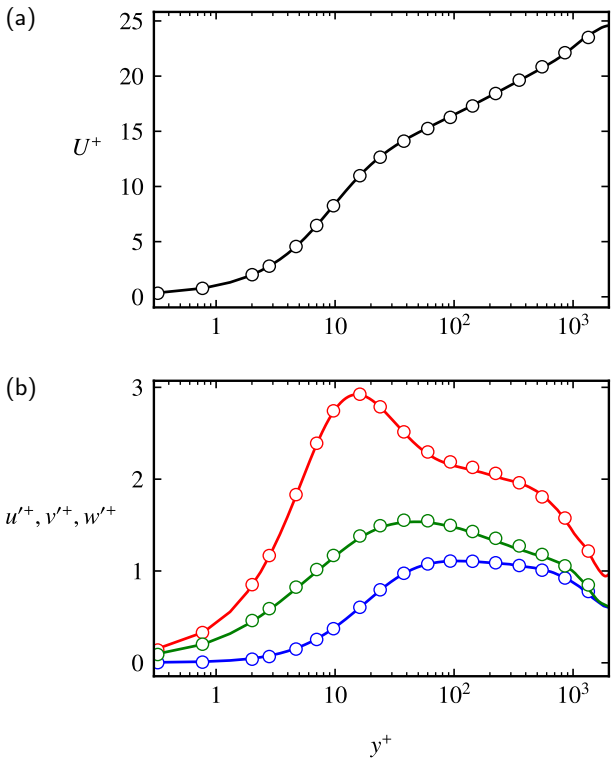

Fig. 1: Wall-normal profiles of (a) the mean streamwise velocity and (b) the streamwise u' (red), wall-normal v' (blue) and spanwise w' (green) root-mean-square values of the fluctuating velocity components. Lines show the present results. The open circles show the results for the same Reynolds number in Hoyas and Jiménez (2008).

light small particles in periodic turbulence at the Taylor-length-based Reynolds number $Re_\lambda = 400$ with systematically changing the relaxation times of particles to show that particles tend to be attracted by vortices whose turnover time is comparable with the relaxation time. Moreover, using the argument by Maxey (1987) under the assumption that particles with the relaxation time τ_p ignore small-scale flow with time scales faster than τ_p, we obtain

$$\boldsymbol{\nabla} \cdot \boldsymbol{v}_p \sim -\tau_p(\beta - 1)Q^{(\sigma)_{cg}}. \tag{1}$$

Here, $\boldsymbol{v}_p$ is the velocity field of the particles when considering them as a continuum and $Q^{(\sigma)_{cg}}$ is the second invariant of the velocity gradient tensor coarse-grained at σ which corresponds to the time scale τ_p. We derive (1) in Appendix A. The parameter β, which will be defined in Section 2.2, is determined by the mass density ratio of the particle and fluid; β is larger (smaller) than unity for light (heavy) particles. Equation (1) implies that heavy particles ($\beta < 1$) are swept out from vortices where $Q^{(\sigma)_{cg}} > 0$, whereas light particles ($\beta > 1$) are attracted by the vortices. Oka et al. (2021) numerically demonstrated the validity of (1) in periodic turbulence. However, it is non-trivial that (1) can describe the clustering in high-Reynolds-number wall turbulence with mean shear.

The purpose of the present study is to understand the fundamental mechanism of the transport of (i) heavy and (ii) light small particles in fully developed turbulent channel flow. In particular, to focus on particle clustering, we conduct DNS of an idealized situation where gravity is negligible and particle size is sufficiently small. This means that the present DNS has limitations in relating the obtained results to real situations. However, by excluding effects of gravity and particle size, we can highlight the role of the hierarchy of coherent structures in the particle clustering. We here propose scenarios of the clustering mechanism of small particles in wall turbulence. As was demonstrated by our previous study (Motoori et al., 2022) on particle dispersions in the turbulence at $Re_\tau = 1000$, (i) heavy particles are swept out predominantly from vortices with the turnover time comparable with the relaxation time. (ii) On the other hand, light particles are likely to be accumulated in the core of vortices with the turnover time comparable with the relaxation time.

In the rest of the present paper, we verify the proposed scenarios by newly conducting DNS of heavy and light small particles in turbulent channel flow at $Re_\tau = 2000$. Although we verified (i) of the scenarios by using turbulence at $Re_\tau = 1000$ (Motoori et al., 2022), in the present study, we show that (i) holds for a higher Reynolds number ($Re_\tau = 2000$). We here emphasize that the chief aim of the present study is to verify (ii) of the scenarios; for this purpose, we conduct DNS of light particles with systematically changing their relaxation time. Moreover, since the clustering condition is similar for the wall-attached and -detached vortices (Motoori et al., 2022), the present study concentrates on the wall-detached vortices. In the following, we briefly explain the numerical simulation methods (Section 2). We then describe the methods of the identification of coherent vortices and their axes (Section 3). By using the identification method, we show the spatial relationships between particles and the hierarchy of coherent vortices (Section 4).

2. Numerical methods

2.1. Direct numerical simulations of turbulence

We numerically simulate turbulent channel flow driven by a constant pressure gradient $\boldsymbol{f}$ by solving the Navier–Stokes equation,

$$\frac{\partial \boldsymbol{u}}{\partial t} + \boldsymbol{u} \cdot \boldsymbol{\nabla}\boldsymbol{u} = -\frac{1}{\rho_f}\boldsymbol{\nabla} p + \nu \nabla^2 \boldsymbol{u} + \boldsymbol{f}, \tag{2}$$

and the continuity equation,

$$\boldsymbol{\nabla} \cdot \boldsymbol{u} = 0. \tag{3}$$

Here, $\boldsymbol{u}(\boldsymbol{x}, t)$ and $p(\boldsymbol{x}, t)$ are the fluid velocity and pressure at position $\boldsymbol{x}$ and time t, respectively; and ρ_f and ν denote the fluid mass density and kinematic viscosity, respectively. Since the target of the present study is a dilute dispersion of small particles, we neglect their effect on fluid motion. For the spatial discretization of the terms in the governing equations, we use a sixth-order central difference scheme

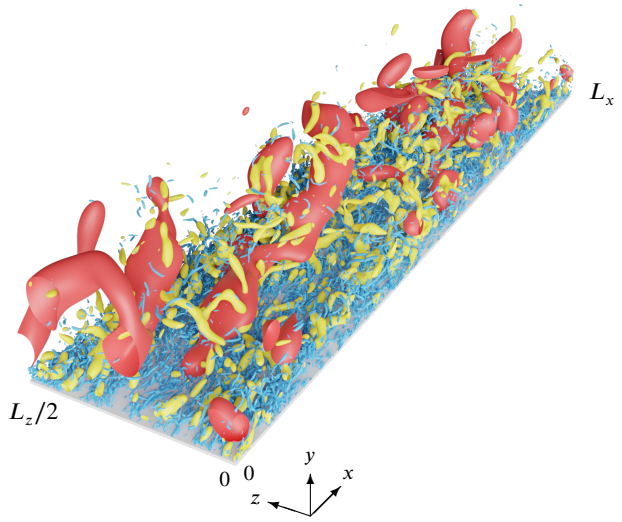

Fig. 2: Hierarchy of vortices identified by the isosurfaces of the second invariant $Q^{(\sigma)}$ of the scale-decomposed velocity gradient tensor at scales $\sigma^+ = 480$ (red), 120 (yellow) and 30 (blue). The thresholds are $Q^{(\sigma)^+} = 1.3\times10^{-6}$ (red), 3.3×10^{-5} (yellow) and 5.0×10^{-4} (blue). We visualize a subdomain (half in the wall-normal direction) of the computational domain.

on a staggered grid in the streamwise (x) and spanwise (z) directions, and use a second-order scheme on the grid with a non-uniform width in the wall-normal (y) direction. We temporally integrate the viscous and convection terms by using the second-order Crank–Nicolson method and the third-order Adams–Bashforth method, respectively. The numerical simulation method is the same as in our previous study (Motoori et al., 2022) but the present Reynolds number is $Re_\tau = 2000$ which is higher than in the previous one ($Re_\tau = 1000$). The numbers of grid points are $(N_x \times N_y \times N_z) = (3072\times1536\times1536)$, and the computational domain size is $(L_x \times L_y \times L_z) = (2\pi h \times 2h \times \pi h)$, where h is the channel half-width.

We show in Fig. 1 the wall-normal distributions of (a) the mean streamwise velocity U and (b) the streamwise u', wall-normal v' and spanwise w' root-mean-square values of the fluctuating velocity. These are in good agreement with the results by Hoyas and Jiménez (2008). Here, $\cdot^+$ denotes the wall units nondimensionalized by u_τ and ν.

2.2. Particle tracking

We assume that particles are spherical and their diameter d_p is sufficiently small so that the particle Reynolds number is sufficiently smaller than unity. We also neglect the gravity and interactions between particles. Under these assumptions, we simulate particles governed by the added mass force and the Stokes drag, that is,

$$\frac{\mathrm{d}\boldsymbol{v}_p}{\mathrm{d}t} = \beta\boldsymbol{a}(\boldsymbol{x}_p,t) - \frac{1}{\tau_p}\big(\boldsymbol{v}_p(t) - \boldsymbol{u}(\boldsymbol{x}_p,t)\big), \tag{4}$$

where $\boldsymbol{x}_p$ and $\boldsymbol{v}_p(=\mathrm{d}\boldsymbol{x}_p/\mathrm{d}t)$ are the position and velocity of a particle, respectively, and $\boldsymbol{a}(\boldsymbol{x},t)$ is the fluid acceleration field. In (4),

$$\beta = \frac{3}{2\rho_p/\rho_f + 1} \tag{5}$$

is the mass factor, where ρ_p denotes the particle mass density, and

$$\tau_p = \frac{\rho_p d_p^2}{18\mu} \tag{6}$$

is the particle velocity relaxation time, where $\mu(=\nu\rho_f)$ denotes the fluid viscosity. Note that the limits of heavy and light particles correspond to $\beta \to 0$ and 3, respectively. To verify the scenarios regarding (i) heavy and (ii) light particles, we simulate two cases with $\beta = 0$ and 3. The another important parameter is the particle relaxation time τ_p (6), the nondimensional form of which is called the Stokes number. We use the Stokes number $St_+ = \tau_p/\tau_+$ nondimensionalized by the wall-unit time-scale $\tau_+(=\nu/u_\tau^2)$, where u_τ is the friction velocity of turbulence. We examine seven cases with $St_+ = 1$, 10, 25, 50, 100, 250 and 1000, which are the same parameters as in Bernardini (2014) and Motoori et al. (2022).

We set $N_p = 10^7$ particles uniform at the initial time ($t = 0$). We follow them by integrating (4) with the second-order Adams–Bashforth method. The fluid velocity at each particle position is estimated by the linear interpolation. In the following analyses, we take the average over the time range of $30 \lesssim t/\tau_L \lesssim 35$ and $4 \lesssim t/\tau_L \lesssim 7$ for heavy and light particles, respectively, where $\tau_L(=h/u_\tau)$ is the turnover time of largest vortices. Since it takes about $50\tau_L$ for heavy particles to accomplish the accumulation to the wall (Bernardini, 2014; Motoori et al., 2022), the particle distribution is not completely equilibrium in the wall-normal direction, although we have confirmed statistical convergence in terms of the clustering in the bulk region for the examined time. Moreover, under the assumption that the particle Reynolds number is smaller than unity, we use the linear Stokes drag in (4), which was used extensively in previous DNS (e.g. Squires and Eaton, 1990, 1991; Yoshimoto and Goto, 2007; Calzavarini et al., 2008; Monchaux et al., 2012; Matsuda et al., 2021; Oka and Goto, 2021; Oka et al., 2021) of turbulence in a periodic cube. Although our previous DNS (Motoori et al., 2022) used an non-linear drag, the results for heavy particles shown below are similar. As mentioned in section 1, we neglect gravity. This assumption can be valid in the bulk region even in realistic situations[1].

3. Scale decomposition of turbulence

To extract the vortices at an arbitrary scale in turbulence, we use a band-pass filter used by our previous studies

[1]For instance, in the case of heavy sands ($\rho_p/\rho_f = 2700$) in air in a channel of a few centimetres, the acceleration ($u_\tau/\tau_p \approx 10^2$–$10^5\,\mathrm{m\,s^{-2}}$ for $St_+ = 1$–1000) due to the Stokes drag is much larger than the gravitational acceleration ($g = 9.8\,\mathrm{m\,s^{-2}}$) in the bulk region. The Kolmogorov acceleration $a_K(=\epsilon^{3/4}/\nu^{1/4})$ is also larger than g, where ϵ is turbulent energy dissipation rate. However, gravity affects the wall accumulation of particles because g is larger than u_τ/τ_p near the wall.

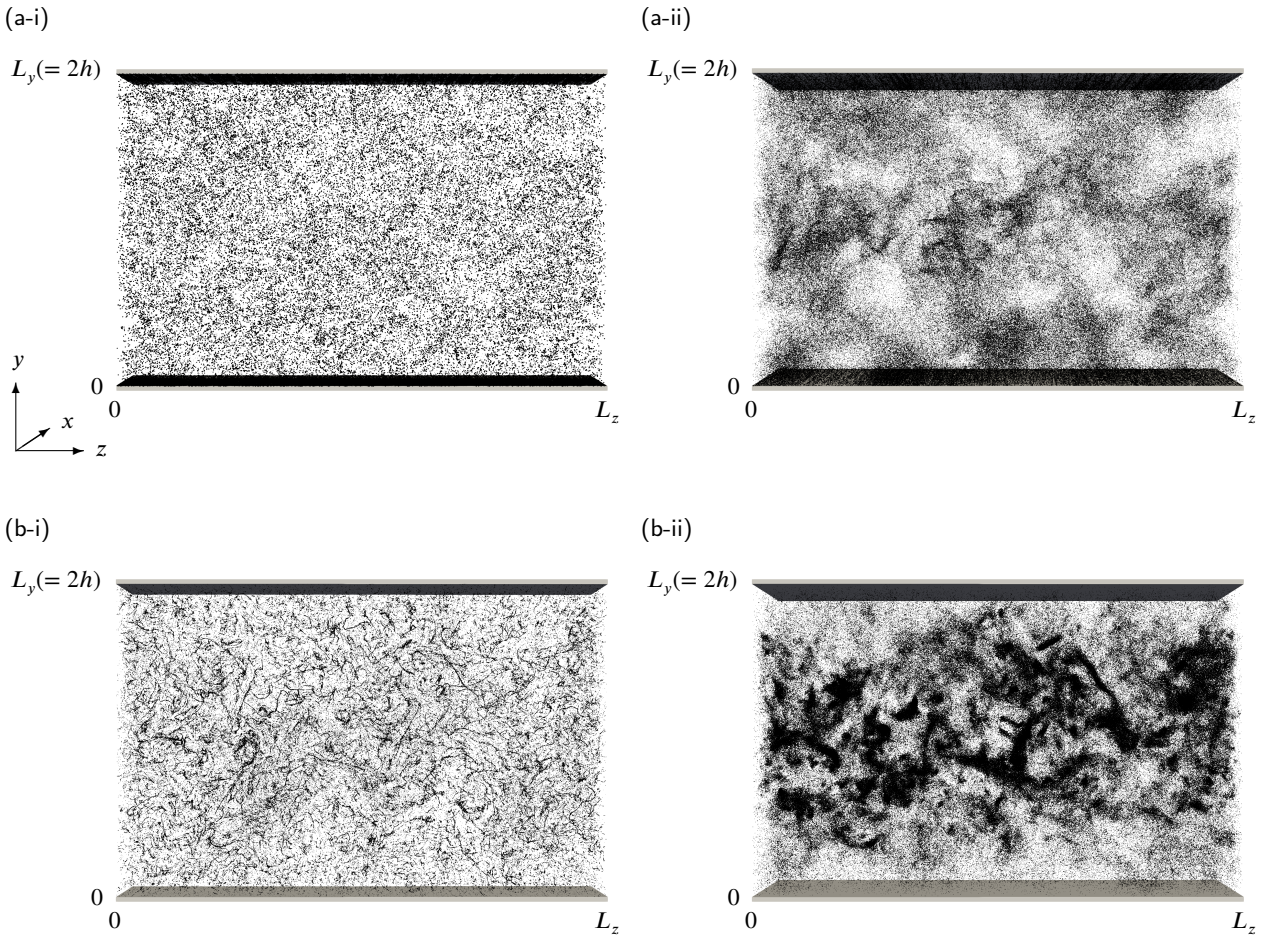

Fig. 3: Spatial distributions of particles with (a) $\beta = 0$ and (b) 3 and different values of the Stokes number: (i) $St_+ = 10$ and (ii) 250. We visualize a subdomain (400 wall units in the streamwise direction) of the computational domain. Supplemental movies 1–4 of the particle distributions with a rotating view shown in the panels (a-i), (a-ii), (b-i) and (b-ii), respectively, are available online.

(Motoori and Goto, 2021; Motoori et al., 2022). Similar scale decomposition for wall turbulence was also used by many authors (e.g. Lee, Lee, Choi and Sung, 2014; Hwang, Lee, Sung and Zaki, 2016; Lozano-Durán, Holzner and Jiménez, 2016; Lee, Sung and Zaki, 2017). In this method, we first apply the Gaussian filter with the filter scale σ to the fluctuating velocity $\check{\boldsymbol{u}}(\boldsymbol{x}, t)$. The obtained velocity $\boldsymbol{u}^{(\sigma)_{cg}}(\boldsymbol{x}, t)$ contains the information of all the scales larger than σ. This implies that the filter corresponds to a low-pass filter of the Fourier modes of the fluctuating velocity. We then take the difference between the low-pass filtered fields at two scales, that is, $\boldsymbol{u}^{(\sigma)}(\boldsymbol{x}, t) = \boldsymbol{u}^{(\sigma)_{cg}}(\boldsymbol{x}, t) - \boldsymbol{u}^{(2\sigma)_{cg}}(\boldsymbol{x}, t)$. This filter corresponds to a band-pass filter of the Fourier modes since $\boldsymbol{u}^{(\sigma)}(\boldsymbol{x}, t)$ contains only the information around the scale σ. In fact, we can confirm that the premultiplied energy spectra have a peak in the wavenumber band corresponding to scales between σ and 2σ.

We here demonstrate that we can capture the hierarchy of vortices by using the scale-decomposed turbulent fields. Figure 2 shows positive isosurfaces of the second invariant $Q^{(\sigma)}$ of the velocity gradient tensor evaluated from $\boldsymbol{u}^{(\sigma)}$ at three scales $\sigma^+ = 30$ (blue), 120 (yellow) and 480 (red). The scale-decomposition reveals clear coherence, that is, the hierarchy of multiscale vortex tubes. Here, $\sigma^+ = 30$ is of the order of size of the smallest vortices, whereas $\sigma^+ = 480$ is approximately the largest ones. As shown in our previous study (Motoori and Goto, 2021), smaller vortices tend to exist around larger ones and they are not parts of larger ones because they are stretched and amplified in the strain-rate fields around larger vortices. Moreover, by applying the low-pressure method (Miura and Kida, 1997; Kida and Miura, 1998) to the band-pass filtered fields, we identify the axes of tubular vortices (see Fig. 3 in Motoori et al., 2022). This method allows us to objectively identify vortices since we do not have to choose a threshold. In the following, we use the axes for the examination of the spatial distribution of particles around vortices with different sizes.

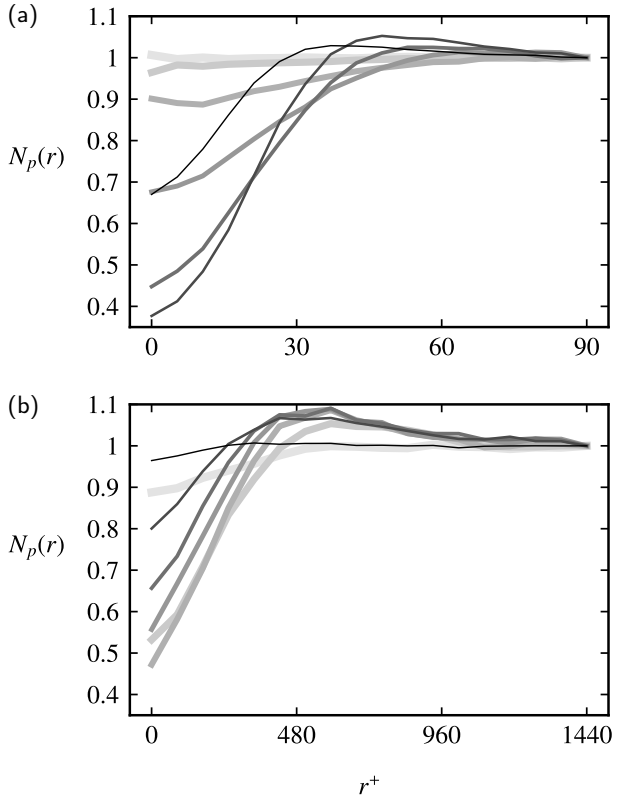

Fig. 4: Average number ratio N_p of heavy particles with $\beta = 0$ existing at distance r from an axis of vortices with sizes (a) $\sigma^+ = 30$ and (b) 480 in the layers (a) $500 \le y^+ < 1000$ and (b) $1500 \le y^+ < 2000$. From the thinner (and darker) to the thicker (and lighter) lines, $St_+ = 1$, 10, 25, 50, 100, 250 and 1000.

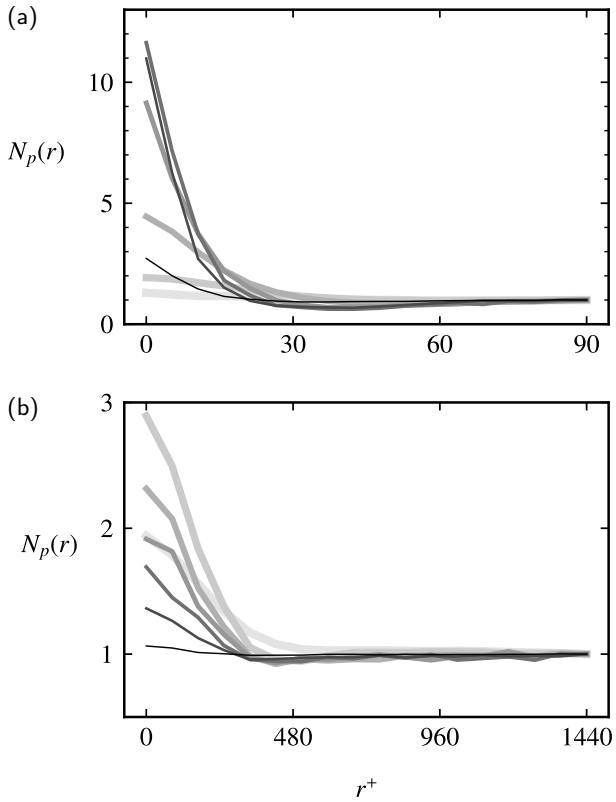

Fig. 5: Same as in Fig. 4 but the results for light ($\beta = 3$) particles.

4. Results

4.1. Visualizations

We show in Fig. 3 the spatial distributions of (a) heavy ($\beta = 0$) and (b) light ($\beta = 3$) particles with (i) $St_+ = 10$ and (ii) 250 at (a) $t \approx 30\tau_L$ and (b) $t \approx 4\tau_L$. We visualize only particles in a thin [(i) 600 and (ii) 1000 wall units] layer in the streamwise direction. The three-dimensional distributions are visualized in supplementary movies 1–4 with a rotating view. In both cases, particles distribute inhomogeneously to form clusters. It is interesting to observe that the cluster shape and size depend on β and St_+, respectively. For heavy ($\beta = 0$) particles, since multiscale tubular vortices contribute to sweeping them out, as was quantitatively demonstrated by our previous study (see Figs. 5 and 6 in Motoori et al., 2022), the clusters of particles are formed around vortices and their size is larger for larger St_+ (Figs. 3a-i and a-ii). In contrast, light ($\beta = 3$) particles seem to form one-dimensional tubular clusters (Figs. 3b-i and b-ii). More precisely, particles with (b-i) $St_+ = 10$ form sharp clusters, whereas particles with (b-ii) $St_+ = 250$ form obscure tubular ones. These observations are more evident in supplemental movies 1–4. The observation for light particles is consistent with the results for turbulence in a periodic cube (Oka et al., 2021). To understand the formation mechanism of the multiscale clustering of heavy and light particles, we quantitatively investigate the relationship between the clustering and the hierarchy of coherent vortices.

4.2. Particle clustering

To quantitatively show the origin of clusters of particles, we identify vortex axes of vortices at each level of the hierarchy. We then evaluate the number of particles around the axis of each vortex. In the following, we evaluate the temporal average of number density N_p^* of particles at the distance r from the vortex axis, and then we show the value $N_p(= N_p^*(r)/N_p^*(r = 3\sigma))$ normalized by that at $r = 3\sigma$ as a function of r. For the results shown in the following, we have confirmed that $N_p^*(r)$ is almost constant for $r \gtrsim 3\sigma$. Therefore, $N_p > 1$ when particles form clusters; whereas $N_p < 1$ when they are sparsely distributed.

4.2.1. Heavy particles

We first show in Fig. 4(a) the average number ratio N_p for heavy ($\beta = 0$) particles around the axes of small-scale ($\sigma^+ = 30$) vortices existing in the layer $500 \le y^+ < 1000$. The thicker (and lighter) lines indicate results for particles with larger St_+. Let us loot at the second thinnest line ($St_+ = 10$). The number ratio takes the minimum at $r = 0$, whereas it takes the maximum around for $\sigma \lesssim r \lesssim 2\sigma$. We can also see

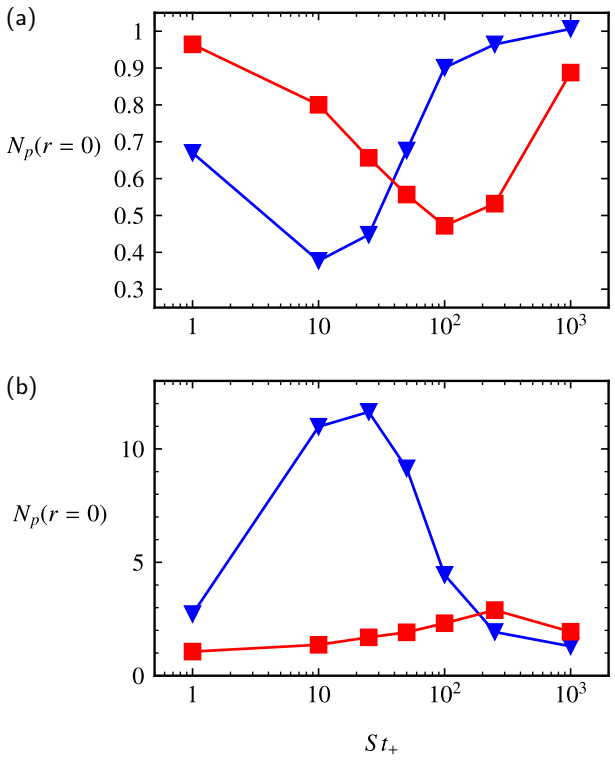

Fig. 6: $N_p(r=0)$ of (a) heavy and (b) light particles on the axes of vortices; namely, we show, in (a) and (b), the values at $r=0$ shown in Figs. 4 and 5, respectively. Blue, $\sigma^+=30$ and $500 \le y^+ < 1000$; red, $\sigma^+=480$ and $1500 \le y^+ < 2000$. The values are shown as functions of St_+.

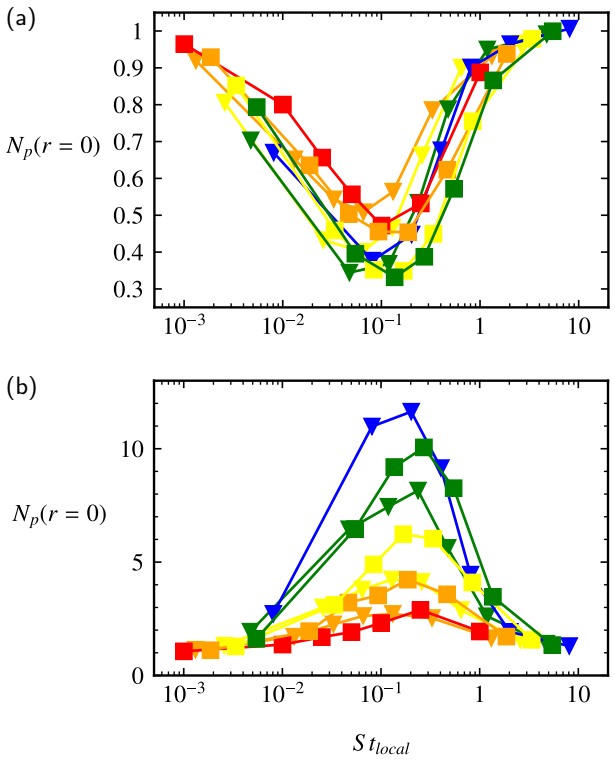

Fig. 7: $N_p(r=0)$ of (a) heavy and (b) light particles on the axes of vortices; same as in Fig. 6 but as functions of St_{local} instead of St_+. We plot $N_p(r=0)$ for the several cases: the different sizes [$\sigma^+=30$ (blue), 60 (green), 120 (yellow), 240 (orange) and 480 (red)], and different layers [$500 \le y^+ < 1000$ (triangles), and $1500 \le y^+ < 2000$ (squares)].

similar tendency for particles with another Stokes number ($St+=25$), which is close to $St_+=10$. On the other hand, N_p for larger $St_+(\gtrsim 100)$ is almost constant independent of r. Hence, in the layer $500 \le y^+ < 1000$, the small-scale ($\sigma^+=30$) wall-detached vortices tend to sweep out particles with $St_+ \approx 10$.

Figure 4(b) shows N_p around vortices with a larger size $\sigma^+=480$ within the layer $1500 \le y^+ < 2000(=h^+)$. We see that particles with $St_+=100$ and 250 are swept out from wall-detached parts ($y > \sigma$) of the large vortices to form a cluster around them. This is consistent with the observation (Fig. 3a-ii) that particles form large clusters. In the previous study (Motoori et al., 2022), which simulated particles subjected to the non-linear Stokes drag, we observed similar clusterings.

4.2.2. Light particles

Next, we numerically verify that light particles with different relaxation times accumulate into different-scale vortices. We show in Fig. 5 the results for light ($\beta=3$) particles. The panel (a) shows the average number ratio N_p around axes of small-scale ($\sigma^+=30$) vortices existing in the layer $500 \le y^+ < 1000$. The values at $r=0$ of the second ($St_+=10$) and third ($St_+=25$) thinnest lines are largest among the seven cases. Away from the axes ($\sigma \lesssim r \lesssim 3\sigma$), N_p is close to unity. This means that light particles with $St_+=10$ and 25 are attracted by vortex axes at the small scale ($\sigma^+=30$). This is consistent with the visualization of particles shown in Fig. 3(b-i).

Figure 5(b) shows N_p around large-scale ($\sigma^+=480$) vortices in the layer $1500 \le y^+ < 2000$. The value at $r=0$ of the second thickest line, which shows the result for $St_+=250$, is the largest among the seven cases. This implies that wall-detached parts of large-scale vortices attract preferentially the particles with $St_+=250$ to their core. Incidentally, comparing the maximum values between in Figs. 5(a) and (b), we see that the attraction degree is stronger for smaller-scale ($\sigma^+=30$) vortices. The result is consistent with the observation shown in Fig. 3(b) that particles with (b-i) $St_+=10$ form sharper clusters than those with (b-ii) $St_+=250$.

4.3. Local Stokes number

In this subsection, we quantitatively show that the time scale matching between particles and vortices is important to explain multiscale clusterings. For this purpose, we first replot, in Fig. 6, N_p at $r=0$ for (a) heavy and (b) light particles as a function of St_+. The blue triangles show the results for $\sigma^+=30$ in the layers $500 \le y^+ < 1000$, whereas the red squares show those for $\sigma^+=480$ in the layers

$1500 \le y^+ < 2000$. In other words, these symbols in panels (a) and (b) show the values at $r = 0$ shown in Figs. 4 and 5, respectively. In both cases, the locations of the minimum and maximum shift to larger St_+ for larger σ^+. This implies that wall-detached vortices with larger sizes tend to clusters of particles with larger St_+; note that the eddy turnover time $T(\sigma, y)$ is determined by $T \sim \sigma^{\frac{2}{3}} y^{\frac{1}{3}}$ in the inertial region in the log layer (Jiménez, 2013; Motoori et al., 2022). The results support the scenarios proposed in the introduction, that is, vortices contributes to the clustering of particles of the relaxation time similar to their eddy turnover time.

Next, we quantitatively show that we can describe the particle clusterings for several sizes and existing heights of vortices in terms of the time scale matching. To this end, we estimate the turnover time $T(\sigma, y)$ of vortices with size σ at height y by $\tau_Q(\sigma, y) = 1/\sqrt{Q^{(\sigma)}_{rms}(y)}$, where $Q^{(\sigma)}_{rms}(y)$ denotes the root-mean-square of the second invariant tensor of the velocity gradient tensor at scale σ. We then define the local Stokes number by

$$St_{local}(\sigma, y) = \frac{\tau_p}{\tau_Q(\sigma, y)}. \tag{7}$$

The vertical values in Fig. 6 are the same as shown in Fig. 7 but shown as functions of St_{local} instead of St_+. Here, we use the value of τ_Q at the centre of each layer. In addition to the two results shown in Fig. 6, we investigate the cases for vortices with different sizes ($\sigma^+ = 30, 60, 120, 240$ and 480) and heights ($500 \le y^+ < 1000$ and $1500 \le y^+ < 2000$), and we plot in Fig. 7 all the results together. Looking at the result for heavy particles in Fig. 7(a), the well of all the curves collapses around $St_{local} \approx 10^{-1}$. For light particles (Fig. 7b), the values for all the lines take the maximum around $St_{local} \approx 10^{-1}$. Hence, irrespective of the height and size, vortices form clusters of heavy and light particles of the relaxation time τ_p comparable with the turnover time τ_Q, which verifies the scenarios proposed in the introduction. These multiscale clusterings around wall-detached ($\sigma < y$) vortices are similar to the observations for heavy (Yoshimoto and Goto, 2007; Oka and Goto, 2021) and light particles in periodic turbulence (Oka et al., 2021). Incidentally, the accumulation rate of particles is lower for particles with the longer relaxation time.

5. Conclusions

To investigate the transport mechanism of heavy and light small particles in high-Reynolds-number turbulent channel flow, we have conducted DNS of those with seven relaxation times ($St_+ = 1$–1000) in the turbulence at $Re_\tau = 2000$. The key ingredient of our analysis is the objective identification of the hierarchy of coherent vortices. We have shown the distribution of particles around the axes of vortices at each level of the hierarchy to show the following. (i) Vortices sweep out predominantly heavy particles with the relaxation time comparable with their turnover time (Fig. 4). (ii) The time scale matching is necessary also for the clustering of light particles; that is to say, vortices attract light particles of the relaxation time comparable with their turnover time (Fig. 5). The multiscale clusterings of particles are determined by the local Stokes number ($St_{local} \approx 10^{-1}$) irrespective of the size and height of coherent vortices (Fig. 7).

The clustering phenomena of heavy particles in the bulk region shown in the present study are similar to those in turbulent channel flow at $Re_\tau = 1000$ (Motoori et al., 2022). Although we did not show the results for light particles in our previous study, the similarity of the heavy particle clusterings implies that the multiscale attractions of light particles are observed irrespective of the Reynolds numbers as long as there is a scale separation in turbulence. This is also the case for the role of wall-attached eddies in the particle clustering, although we concentrate on the wall-detached eddies in the present study. More precisely, irrespective of Re_τ, heavy particles are swept out from streamwise vortices with the time scale matching with τ_p, being accumulated in low-speed streaks; whereas light particles are attracted by the vortices.

Incidentally, it is also necessary for the clustering that the lifetime T_{life} of vortices is longer than the clustering time $T_{cluster}$. Estimating $Q^{(\sigma)_{cg}}$ by τ_Q^{-2} in (1), we can evaluate the clustering time as

$$T_{cluster} \approx \frac{\tau_Q^2}{\tau_p |1 - \beta|}. \tag{8}$$

Therefore, a necessary condition of clustering is

$$T_{cluster} \lesssim T_{life} \;\Leftrightarrow\; \frac{\tau_Q^2(\sigma, y)}{T_{life}(\sigma, y)} \lesssim \tau_p |1 - \beta|. \tag{9}$$

If we assume that the lifetime is comparable with the turnover time of vortices ($T_{life} \approx \tau_Q$), we obtain $St_{local} \approx 1$; note that (1) holds when $\tau_p \lesssim \tau_Q$ (see Oka et al. 2021 and Appendix A). This is the reason why time scale matching is important for particle clustering.

Before closing the present article, we must note that we have assumed that the particle diameter d_p is small enough for the particle Reynolds number to be sufficiently smaller than unity. In the case of light particles, although the assumption is violated when τ_p is large, as was shown by Oka et al. (2021), the clustering condition (1) can be valid for $d_p < \sigma$, because vortices smaller than σ do not much contribute to the particle clustering. This is the reason why large light particles such as air bubbles and silica aerogel particles can form cluster in large vortices (see the discussion by Oka et al., 2021). In addition, the present DNS, where we assume the linear Stokes drag and neglect gravity, can be discrepant from realistic situations[2]. Although there are limitations in the applicability of the present results to real situations, the present study has revealed the substance of

[2]For example, if we assume heavy sands ($\rho_p/\rho_f = 2700$) in air, we can estimate from the present DNS results that the particle Reynolds number for $St_+ = 1000$ is about 5 around the channel center, which is inconsistent with the linear Stokes drag law.

particle clustering by the hierarchy of coherent vortices. As mentioned in the introduction, the recent experiment (Berk and Coletti, 2020) also demonstrated qualitatively similar clustering phenomena for heavy particles in a wide range of St_+ in high-Reynolds-number turbulent boundary layers. Therefore, the present analysis of the ideal system helps to understand the essence behind particle clustering phenomena observed in more realistic systems.

Acknowledgements

This study was partly supported by the JSPS Grants-in-Aid for Scientific Research 20H02068, 21K20403 and 23K13253. The DNS were conducted under the auspices of the NIFS Collaboration Research Programs (NIFS22KISS010) and under the supercomputer Fugaku provided by RIKEN through the HPCI System Research projects (hp210207 and hp220232).

A. Derivation of (1)

In this appendix, we derive (1). Similar explanations are in Oka et al. (2021). We first assume that the motion of particles with τ_p is independent of fluid motions smaller than σ, where σ is the length scale such that the turnover time $T(\sigma)$ of eddies with size σ is about τ_p. This is because they cannot follow the fluid motion faster than τ_p. We can therefore assume that the motion of the particles is similar to that of the imaginary particles which obey

$$\frac{\mathrm{d}\boldsymbol{v}_c}{\mathrm{d}t} = \beta \boldsymbol{a}^{(\sigma)_{cg}}(\boldsymbol{x}_c, t) - \frac{1}{\tau_p}\left(\boldsymbol{v}_c(t) - \boldsymbol{u}^{(\sigma)_{cg}}(\boldsymbol{x}_c, t)\right). \quad (10)$$

Here, $\boldsymbol{u}^{(\sigma)_{cg}}$ and $\boldsymbol{a}^{(\sigma)_{cg}}$ are fluid velocity and acceleration coarse-grained at σ, respectively, and, $\boldsymbol{x}_c$ and $\boldsymbol{v}_c$ are the position and velocity of an imaginary particle, respectively. Then, we apply the argument of Maxey (1987) to (10) to obtain the velocity difference between the fluid and particle,

$$\boldsymbol{v}_c - \boldsymbol{u}^{(\sigma)_{cg}}(\boldsymbol{x}_c, t) = \tau_p(\beta - 1)\boldsymbol{a}^{(\sigma)_{cg}}(\boldsymbol{x}_c, t). \quad (11)$$

Note that (11) holds when $\tau_p \lesssim T(\sigma)$. Taking the divergence of (11), we obtain

$$\boldsymbol{\nabla} \cdot \boldsymbol{v}_c = \tau_p(\beta - 1)\boldsymbol{\nabla} \cdot \boldsymbol{a}^{(\sigma)_{cg}}(\boldsymbol{x}_c, t). \quad (12)$$

Here, we have also assumed that we can define the particle velocity field, which is a smooth function of $\boldsymbol{x}$. Then, if σ is in the inertial range, we can approximate $\boldsymbol{a}^{(\sigma)_{cg}}$ by $-(1/\rho_f)\boldsymbol{\nabla} p^{(\sigma)_{cg}}$ where we define $p^{(\sigma)_{cg}}$ as the solution of the Poisson equation:

$$\nabla^2 p^{(\sigma)_{cg}} = -\rho_f \boldsymbol{\nabla} \cdot (\boldsymbol{u}^{(\sigma)_{cg}} \cdot \boldsymbol{\nabla} \boldsymbol{u}^{(\sigma)_{cg}}) = \rho_f Q^{(\sigma)_{cg}}. \quad (13)$$

Substituting this approximation and (13) into (12), we obtain (1).

References

Balachandar, S., Eaton, J.K., 2010. Turbulent dispersed multiphase flow. Annu. Rev. Fluid Mech. 42, 111–133.

Berk, T., Coletti, F., 2020. Transport of inertial particles in high-Reynolds-number turbulent boundary layers. J. Fluid Mech. 903, A18.

Bernardini, M., 2014. Reynolds number scaling of inertial particle statistics in turbulent channel flows. J. Fluid Mech. 758, R1.

Brandt, L., Coletti, F., 2022. Particle-laden turbulence: progress and perspectives. Annu. Rev. Fluid Mech. 2022 54, 159–189.

Calzavarini, E., Kerscher, M., Lohse, D., Toschi, F., 2008. Dimensionality and morphology of particle and bubble clusters in turbulent flow. J. Fluid Mech. 607, 13–24.

Caporaloni, M., Tampieri, F., Trombetti, F., Vittori, O., 1975. Transfer of particles in nonisotropic air turbulence. J. Atmos. Sci. 32, 565–568.

Douady, S., Couder, Y., Brachet, M.E., 1991. Direct observation of the intermittency of intense vorticity filaments in turbulence. Phys. Rev. Lett. 67, 983.

Gustavsson, K., Mehlig, B., 2016. Statistical models for spatial patterns of heavy particles in turbulence. Adv. Phys. 65, 1–57.

Guzzella, L., Onder, C., 2009. Introduction to modeling and control of internal combustion engine systems. Springer Science & Business Media.

Hoyas, S., Jiménez, J., 2008. Reynolds number effects on the Reynolds-stress budgets in turbulent channels. Phys. Fluids 20, 101511.

Hwang, J., Lee, J., Sung, H.J., Zaki, T.A., 2016. Inner-outer interactions of large-scale structures in turbulent channel flow. J. Fluid Mech. 790, 128–157.

Jie, Y., Cui, Z., Xu, C., Zhao, L., 2022. On the existence and formation of multi-scale particle streaks in turbulent channel flows. J. Fluid Mech. 935, A18.

Jiménez, J., 2013. Near-wall turbulence. Phys. Fluids 25, 101302.

Johnson, P.L., Bassenne, M., Moin, P., 2020. Turbophoresis of small inertial particles: theoretical considerations and application to wall-modelled large-eddy simulations. J. Fluid Mech. 883, A27.

Kida, S., Miura, H., 1998. Identification and analysis of vortical structures. Eur. J. Mech. B/Fluids 17, 471–488.

Lakehal, D., Métrailler, D., Reboux, S., 2017. Turbulent water flow in a channel at $Re_\tau = 400$ laden with 0.25 mm diameter air-bubbles clustered near the wall. Phys. Fluids 29, 065101.

Lee, J., Lee, J.H., Choi, J.I., Sung, H.J., 2014. Spatial organization of large- and very-large-scale motions in a turbulent channel flow. J. Fluid Mech. 749, 818–840.

Lee, J., Sung, H.J., Zaki, T.A., 2017. Signature of large-scale motions on turbulent/non-turbulent interface in boundary layers. J. Fluid Mech. 819, 165–187.

Lozano-Durán, A., Holzner, M., Jiménez, J., 2016. Multiscale analysis of the topological invariants in the logarithmic region of turbulent channels at a friction Reynolds number of 932. J. Fluid Mech. 803, 356–394.

Marchioli, C., Giusti, A., Salvetti, M.V., Soldati, A., 2003. Direct numerical simulation of particle wall transfer and deposition in upward turbulent pipe flow. Int. J. Multiph. Flow 29, 1017–1038.

Marchioli, C., Soldati, A., 2002. Mechanisms for particle transfer and segregation in a turbulent boundary layer. J. Fluid Mech. 468, 283–315.

Matsuda, K., Schneider, K., Yoshimatsu, K., 2021. Scale-dependent statistics of inertial particle distribution in high Reynolds number turbulence. Phys. Rev. Fluids 6, 064304.

Maxey, M.R., 1987. The gravitational settling of aerosol particles in homogeneous turbulence and random flow fields. J. Fluid Mech. 174, 441–465.

Miura, H., Kida, S., 1997. Identification of tubular vortices in turbulence. J. Phys. Soc. Jpn. 66, 1331–1334.

Monchaux, R., Bourgoin, M., Cartellier, A., 2012. Analyzing preferential concentration and clustering of inertial particles in turbulence. Int. J. Multiph. Flow 40, 1–18.

Motoori, Y., Goto, S., 2021. Hierarchy of coherent structures and real-space energy transfer in turbulent channel flow. J. Fluid Mech. 911, A27.

Motoori, Y., Wong, C., Goto, S., 2022. Role of the hierarchy of coherent structures in the transport of heavy small particles in turbulent channel

flow. J. Fluid Mech. 942, A3.
Narayanan, C., Lakehal, D., Botto, L., Soldati, A., 2003. Mechanisms of particle deposition in a fully developed turbulent open channel flow. Phys. Fluids 15, 763–775.
Oka, S., Goto, S., 2021. Generalized sweep-stick mechanism of inertial-particle clustering in turbulence. Phys. Rev. Fluids 6 , 044605.
Oka, S., Watanabe, D., Goto, S., 2021. Large-scale clustering of light small particles in developed turbulence. Phys. Fluids 33, 285.
Park, H.J., Saito, D., Tasaka, Y., Murai, Y., 2019. Color-coded visualization of microbubble clouds interacting with eddies in a spatially developing turbulent boundary layer. Exp. Therm. Fluid Sci. 109, 109919.
Picano, F., Sardina, G., Casciola, C.M., 2009. Spatial development of particle-laden turbulent pipe flow. Phys. Fluids 21, 093305.
Picciotto, M., Marchioli, C., Soldati, A., 2005. Characterization of near-wall accumulation regions for inertial particles in turbulent boundary layers. Phys. Fluids 17, 098101.
Reeks, M.W., 1983. The transport of discrete particles in inhomogeneous turbulence. J. Aero. Sci. 14, 729–739.
Riley, J.J., Patterson, G.S., 1974. Diffusion experiments with numerically integrated isotropic turbulence. Phys. Fluids 17, 292–297.
Saito, I., Gotoh, T., 2018. Turbulence and cloud droplets in cumulus clouds. New J. Phys. 20, 023001.
Sardina, G., Schlatter, P., Brandt, L., Picano, F., Casciola, C.M., 2012. Wall accumulation and spatial localization in particle-laden wall flows. J. Fluid Mech. 699, 50–78.
Scherer, M., Uhlmann, M., Kidanemariam, A.G., Krayer, M., 2022. On the role of turbulent large-scale streaks in generating sediment ridges. J. Fluid Mech. 930, A11.
Seminara, G., 2010. Fluvial sedimentary patterns. Annu. Rev. Fluid Mech. 42, 43–66.
Shaw, R.A., 2003. Particle-turbulence interactions in atmospheric clouds. Annu. Rev. Fluid Mech. 35, 183–227.
Soldati, A., Marchioli, C., 2009. Physics and modelling of turbulent particle deposition and entrainment: Review of a systematic study. Int. J. Multiph. Flow 35, 827–839.
Squires, K.D., Eaton, J.K., 1990. Particle response and turbulence modification in isotropic turbulence. Phys. Fluids A 2, 1191–1203.
Squires, K.D., Eaton, J.K., 1991. Preferential concentration of particles by turbulence. Phys. Fluids A 3, 1169–1178.
Tagawa, Y., Mercado, J.M., Prakash, V.N., Calzavarini, E., Sun, C., Lohse, D., 2012. Three-dimensional Lagrangian Voronoï analysis for clustering of particles and bubbles in turbulence. J. Fluid Mech. 693, 201–215.
Toschi, F., Bodenschatz, E., 2009. Lagrangian properties of particles in turbulence. Annu. Rev. Fluid Mech. 41, 375–404.
Vaillancourt, P.A., Yau, M.K., 2000. Review of Particle-Turbulence Interactions and Consequences for Cloud Physics. Bull. Am. Met. Soc. 81.
Yeung, P.K., 2002. Lagrangian investigations of turbulence. Annu. Rev. Fluid Mech. 34, 115–142.
Yoshimoto, H., Goto, S., 2007. Self-similar clustering of inertial particles in homogeneous turbulence. J. Fluid Mech. 577, 275–286.
Zhai, J., Fairweather, M., Colombo, M., 2020. Simulation of microbubble dynamics in turbulent channel flows. Flow Turbul. Combust. 105, 1303–1324.